

# A Two-Step Procedure to Detect Cosmological Gravitational Wave Backgrounds with Next-Generation Terrestrial Gravitational-Wave Detectors

Haowen Zhong <sup>1,\*</sup>, Luca Reali <sup>2,†</sup>, Bei Zhou <sup>3,4,‡</sup>, Emanuele Berti <sup>2,§</sup> and Vuk Mandic <sup>1,¶</sup>

<sup>1</sup>*School of Physics and Astronomy, University of Minnesota, Minneapolis, MN 55455, USA*

<sup>2</sup>*William H. Miller III Department of Physics and Astronomy,  
Johns Hopkins University, Baltimore, Maryland 21218, USA*

<sup>3</sup>*Theory division, Fermi National Accelerator Laboratory, Batavia, Illinois 60510, USA*

<sup>4</sup>*Kavli Institute for Cosmological Physics, University of Chicago, Chicago, Illinois 60637, USA*

(Dated: January 30, 2025)

Cosmological gravitational-wave backgrounds are an exciting science target for next-generation ground-based detectors, as they encode invaluable information about the primordial Universe. However, any such background is expected to be obscured by the astrophysical foreground from compact-binary coalescences. We propose a novel framework to detect a cosmological gravitational-wave background in the presence of binary black holes and binary neutron star signals with next-generation ground-based detectors, including Cosmic Explorer and the Einstein Telescope. Our procedure involves first removing all the individually resolved binary black hole signals by notching them out in the time-frequency domain. Then, we perform joint Bayesian inference on the individually resolved binary neutron star signals, the unresolved binary neutron star foreground, and the cosmological background. For a flat cosmological background, we find that we can claim detection at  $5\sigma$  level when  $\Omega_{\text{ref}} \geq 2.7 \times 10^{-12} / \sqrt{T_{\text{obs}}/\text{yr}}$ , where  $T_{\text{obs}}$  is the observation time (in years), which is within a factor of  $\lesssim 2$  from the sensitivity reached in absence of these astrophysical foregrounds.

**Introduction.** The next generation (XG) of ground-based gravitational-wave (GW) detectors, such as Cosmic Explorer (CE) [1–3] and the Einstein Telescope (ET) [4, 5], will see an unprecedented increase in sensitivity both to individual compact binary coalescence (CBC) events and to stochastic signals. This will allow us to individually resolve nearly all of the binary black hole (BBH) mergers and a significant fraction of binary neutron star (BNS) and neutron star-black hole (NSBH) events in the entire Universe [6, 7]. Furthermore, we will probe the stochastic gravitational wave backgrounds (SGWBs) across several orders of magnitude in amplitude [8, 9]. In particular, the detection of a cosmological gravitational wave background (CGWB) would open up a unique window to observe the earliest moments of the Universe and probe physics at energies close to the Planck scale [10–17]. This detection is challenging because of the simultaneous presence of the SGWBs from CBCs, which effectively act as a foreground, limiting the sensitivity to other subdominant SGWBs [18].

Several methods have been proposed to bypass the CBC foreground. Given the high fraction of individually resolved CBC signals with XG detectors, one could simply fit and subtract them from the data in the frequency domain to lower the foreground [8, 19]. However, the recovery of detected signals is never perfect, and the pile-up of residuals from imperfect subtraction can produce an effective foreground that is comparable to the original SGWB before removal [20–22]. Techniques have been proposed to further reduce this effective foreground in the frequency domain, from applying a projection method [23, 24] to estimating and subtracting the expected residual power [25]. Ref. [26] showed that subtraction

results in the frequency domain are actually significantly more optimistic if one abandons the linear-signal approximation in favor of more realistic estimates of the residuals. On the other hand, Refs. [27, 28] proposed a time-frequency approach to notch-out the detected signals by masking the associated pixels. They showed that this method could reduce the CBC foreground by one order of magnitude even when residuals from imperfect recovery are taken into account [28].

All of the aforementioned techniques can only lower the CBC foreground by removing individually resolved CBC signals, but the sensitivity to subdominant SGWBs would still be limited by the BNS signals that are too weak to be individually detected, where the unresolvable BNS foreground is about at the order of  $\mathcal{O}(10^{-11})$  at  $f_{\text{ref}} = 25\text{Hz}$  [28, 29]. Refs. [30–32] proposed a Bayesian framework to simultaneously fit all of the CBC signals without distinguishing between resolved and unresolved. Ref. [33] suggested using the information on the CBC population from detected events to predict the foreground from unresolved signals and remove it from the data. While promising, the computational feasibility of these methods with a realistic number of events in the context of XG detectors has yet to be proven.

In this Letter, we propose a novel method that combines the notching procedure of Refs. [27, 28] with the joint hierarchical inference of Ref. [34]. First, we notch out all the detected BBH signals, showing that the residual BBH foreground is negligible. Then, we jointly fit within a unified Bayesian framework the resolved BNS events, the foreground from unresolved BNS events, and a CGWB. For illustration, we apply this procedure to mock data including realistic BBH and BNS populations

and a flat CGWB.

**Astrophysical population and setup.** For both BBHs and BNSs, we assume the same population models as in Refs. [27, 28]. We employ the `PowerLaw+Peak` model from the latest LIGO-Virgo-KAGRA (LVK) catalog [35] to characterize the BBH mass distribution, while we assume that the BNS masses are uniformly distributed within the range  $[1, 2] M_\odot$  [35, 36]. We assume zero spins and an isotropic distribution of the orbital orientation and sky position for all the binaries. To obtain the redshift distribution, we convolve the star formation rate (SFR) [37]

$$R_f(z) = \mathcal{N} \frac{ae^{b(z-z_p)}}{a - b + be^{a(z-z_p)}} \quad (1)$$

with a power-law time delay distribution  $p(t_d) \propto t_d^p$  with  $p = -1$ . The source-frame merger rate  $R_m(z)$  then reads

$$R_m(z) = \int_{t_{\min}}^{t_{\max}} R_f(z_f) p(t_d) dt_d, \quad (2)$$

where  $z_f = z[t(z) - t_d]$  is the binary formation time, we set  $t_{\min} = 20$  Myr for BNSs and 50 Myr for BBHs, and we set  $t_{\max}$  to be the Hubble time in both cases. We fix the parameters in the SFR to  $z_p = 2.00$ ,  $a = 2.37$  and  $b = 1.80$  [37], while  $\mathcal{N}$  is a normalization factor chosen so that the local merger rate  $\mathcal{R}_0$  is consistent with the LVK results [35]. In particular, for BNSs we set  $\mathcal{R}_0 = 320 \text{ Gpc}^{-3} \text{ yr}^{-1}$ ; for BBHs, we choose a value of  $\mathcal{R}_0$  such that  $\mathcal{R}_m(z = 0.2) = 28.1 \text{ Gpc}^{-3} \text{ yr}^{-1}$  [35].

Besides the CBC signals, we also simulate a power-law CGWB

$$\Omega_{\text{GW}}(f) = \Omega_{\text{ref}} \left( \frac{f}{f_{\text{ref}}} \right)^\alpha, \quad (3)$$

where we choose  $\alpha = 0$  and  $\Omega_{\text{ref}} = 2.0 \times 10^{-11}$  at  $f_{\text{ref}} = 25$  Hz. Our framework is not fundamentally limited by the exact functional form of the CGWB, and we choose a simple flat CGWB for demonstration purposes.

We consider a network of XG interferometers composed of two 40-km long CE detectors located at the LIGO Livingston and LIGO Hanford sites [38], and an ET detector located at the Virgo site [39]. We assume Gaussian and stationary detector noise, modeled via a perfectly known power spectral density (PSD) and uncorrelated among different detectors. For both CE detectors, we adopt the PSD curve of Ref. [6], while for ET we assume the PSD of the triangular configuration in Ref. [5]. We set the low-frequency sensitivity limit to be 5 Hz for all detectors in the network.

We use `Bilby` [40] to simulate and add detector noise and CBC signals into a time series. For BBH signals, we

adopt the `IMRPhenomXAS` waveform model [41], which is a full inspiral-merger-ringdown, non-precessing waveform model for the fundamental mode. For BNS signals we use the inspiral-only `TaylorT4` waveform model [42], as we expect most of the BNS signals in XG detectors to be inspiral-dominated.

We use `pygwb` [43] to simulate and add the CGWB into the time series and compute cross-correlations for the stochastic search. With our network of XG detectors, Ref. [28] showed that combining cross-correlation results from all ten possible baselines yields an improvement in the sensitivity of the stochastic search of less than 10% compared to using a single baseline of two CE detectors. Using all baselines would require 10 times more computational power. Therefore, for demonstration purposes, here we only cross-correlate time series data from two CE interferometers.

**Data-analysis method.** We devise a procedure that combines the notching method of Refs. [27, 28] with the joint Bayesian inference of Ref. [34].

We assess the detectability of individual CBC signals by computing their network signal-to-noise ratio (SNR) [44], choosing detection thresholds of  $\text{SNR}_{\text{thr}}^{\text{BBH}} = 8$  for BBHs and  $\text{SNR}_{\text{thr}}^{\text{BNS}} = 12$  for BNSs [28]. With the population model we adopt, we find that 99.7% of the BBH and 50.4% of the BNS signals are detected given two CE and one ET detectors network. We then apply the time-frequency approach of Ref. [28] to notch out all the detected BBH signals from the data. As we show below, the remaining BBH foreground, resulting from the combination of the few unresolved BBH signals and the residuals from imperfect removal, is weaker than the network sensitivity; hence, we do not include it in the inference studies.

After applying this notching procedure, the data contains only BNS signals and the CGWB. If we followed Ref. [28] and notched out the resolved BNS events as well, we would still be limited by the foreground from unresolved BNS signals. Instead, we adopt the Bayesian framework of Ref. [34] to jointly fit the resolved BNS signals along with the BNS foreground and the CGWB. Ref. [34] devised this method in the context of current LVK detectors, where the SGWB complements the hierarchical inference on individually resolved events by providing information on the CBC population at high redshift [35]. Here, instead, the information from detected events helps us tighten the constraints on the BNS foreground and distinguish it from the CGWB.

Let us consider a set of data segments  $\{\mathbf{d}_i\}_{i=1}^{N_{\text{obs}}}$  from  $N_{\text{obs}}$  individual BNS detections and the cross-correlation spectrum  $\hat{C}^*(f)$  after notching out the resolvable BBH signals (see the Supplement for the definition of  $\hat{C}^*(f)$ ). Their joint likelihood can be written as [34]

$$\mathcal{L}(\{\mathbf{d}_i\}_{i=1}^{N_{\text{obs}}}, \hat{C}^*(f) | \mathbf{\Lambda}_{\text{BNS}}, \mathbf{\Lambda}_{\text{CGWB}}) = \mathcal{L}_{\text{BNS}}(\{\mathbf{d}_i\}_{i=1}^{N_{\text{obs}}} | \mathbf{\Lambda}_{\text{BNS}}) \times \mathcal{L}_{\text{SGWB}}(\hat{C}^*(f) | \mathbf{\Lambda}_{\text{BNS}}, \mathbf{\Lambda}_{\text{CGWB}}), \quad (4)$$

where  $\mathcal{L}_{\text{BNS}}(\{\mathbf{d}_i\}_{i=1}^{N_{\text{obs}}}|\mathbf{\Lambda}_{\text{BNS}})$  is the usual hierarchical likelihood for population inference on the detected events [45, 46], while  $\mathcal{L}_{\text{SGWB}}(\hat{C}^*(f)|\mathbf{\Lambda}_{\text{BNS}}, \mathbf{\Lambda}_{\text{CGWB}})$  is the Gaussian likelihood for stochastic searches [47, 48]. Here  $\mathbf{\Lambda}_{\text{CGWB}} = \{\Omega_{\text{ref}}, \alpha\}$  encodes the parameters characterizing the CGWB, while  $\mathbf{\Lambda}_{\text{BNS}}$  is the set of hyperparameters defining the BNS population, which affect both the individually detected events and the SGWB from unresolved BNS signals. To simplify the inference, we assume that the BNS mass distribution is perfectly known and that the angular parameters are isotropically distributed. Hence, the only BNS hyperparameters  $\mathbf{\Lambda}_{\text{BNS}}$  that we are inferring are the ones characterizing the redshift distribution. In particular, we consider two cases:

- 1) A simplistic *known SFR* scenario where we assume that the SFR is completely known, and all that is left to determine are the local merger rate,  $\mathcal{R}_0$ , and the power-law index of the time-delay distribution,  $p$ . Then the joint inference involves a total of four parameters  $\{\mathbf{\Lambda}_{\text{BNS}}, \mathbf{\Lambda}_{\text{CGWB}}\} = \{\mathcal{R}_0, p, \Omega_{\text{ref}}, \alpha\}$ .
- 2) A more realistic *unknown SFR* scenario where we assume no prior knowledge of the redshift distribution, except for its functional form. Following the approach of Ref. [49], we assume that the merger rate has the same functional form as the SFR of Eq. (1), then we fit this function to the merger rate  $R_m(z)$  computed via Eq. (2) to obtain the injected values  $a_{\text{inj}} = 2.15$ ,  $b_{\text{inj}} = 1.40$ ,  $z_p^{\text{inj}} = 1.64$ . In this case, we directly infer these parameters along with the local merger rate  $\mathcal{R}_0$ , so the joint inference involves a total of six parameters  $\{\mathbf{\Lambda}_{\text{BNS}}, \mathbf{\Lambda}_{\text{CGWB}}\} = \{\mathcal{R}_0, a, b, z_p, \Omega_{\text{ref}}, \alpha\}$ .

Performing full Bayesian parameter estimation (PE) on thousands of individually resolved BNS signals is currently computationally unfeasible. Hence, we generate synthetic samples for the individual BNS likelihoods on source parameters using the approximate method of Refs. [34, 50]. For the exact expressions of the joint likelihood and additional details on the inference procedure, we refer the reader to the Supplemental Material.

**Joint inference results.** For demonstration purposes, we perform our analysis assuming an observation time  $T_{\text{obs}} = 10$  days. With our population model, this corresponds to roughly  $\sim 650$  BBH signals that we notch out, and  $\sim 7000$  resolvable BNS events that enter the hierarchical likelihood  $\mathcal{L}_{\text{BNS}}(\{\mathbf{d}_i\}_{i=1}^{N_{\text{obs}}}|\mathbf{\Lambda}_{\text{BNS}})$ .

In vanilla searches for a single, dominant SGWB, its SNR is straightforward to compute, and it is a good figure of merit to estimate whether the target SGWB is strong enough to be detectable relative to the detector noise [35, 51, 52]. In our case, instead, we are jointly fitting for the BNS hyperparameters from individually detected sources plus two distinct SGWBs, and our target is, in fact, the subdominant CGWB. Hence, we turn

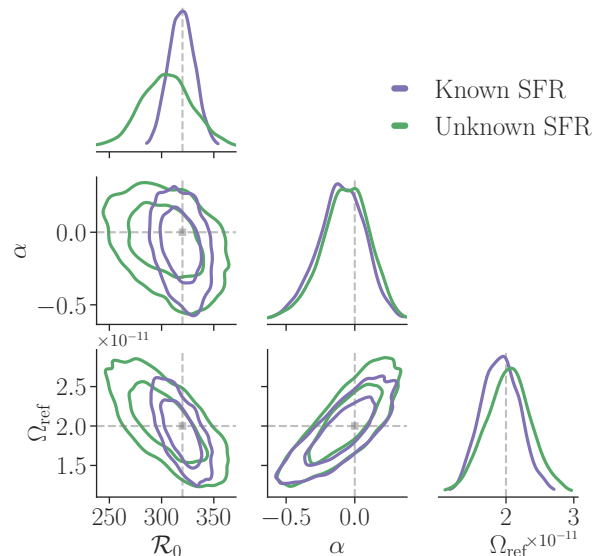


FIG. 1. Marginalized Joint posterior distributions on  $\{\mathcal{R}_0, \alpha, \Omega_{\text{ref}}\}$  for the models assuming known SFR (purple curves) and unknown SFR (green curves). Contours enclose 68% and 95% of the probability mass. Gray dashed lines indicate the true simulated values of parameters.

to a full Bayesian approach and we study the inferred posterior to find evidence for CGWB detection.

In both our scenarios, we find that the posteriors on all the parameters are fully consistent with the simulated values. In Fig. 1, we compare the joint posteriors on the common parameters for both inferences, namely the CGWB parameters  $\{\Omega_{\text{ref}}, \alpha\}$  and the local BNS merger rate  $\mathcal{R}_0$ . As expected, we find that assuming better knowledge of the BNS redshift distribution has a large impact on inferring the local merger rate. The 95% confidence interval on  $\mathcal{R}_0$  roughly doubles going from known (purple curves) to unknown (green curves) SFR.

However, the joint posterior on  $\{\alpha, \Omega_{\text{ref}}\}$  is remarkably similar in both analyses, indicating that adding more parameters to our inference of the BNS redshift distribution does not have a large impact on the inference of the CGWB. Crucially, we find that we can confidently claim the detection of the CGWB in both scenarios: we exclude  $\Omega_{\text{ref}} = 0$  at the  $6.8\sigma$  level assuming known SFR and at  $6.1\sigma$  level with unknown SFR. We refer to Table I for the marginalized posterior distributions of all parameters in the different cases.

In Fig. 2, we further compare the marginalized posterior distributions on  $\{\Omega_{\text{ref}}, \alpha\}$  from our two joint-inference scenarios (purple and green curves) with the posterior from an ideal search for the CGWB where no CBC foreground is present (orange curves). In other words, the ideal search corresponds to a benchmark case where only the CGWB is simulated, and the second term of Eq. (4) in the form  $\mathcal{L}_{\text{SGWB}}(\hat{C}^*(f)|\mathbf{\Lambda}_{\text{CGWB}})$  is used for the inference. After applying our notching+joint infer-

TABLE I. Marginalized posterior distribution (median and 95% credible symmetric interval).

Scenario	$\mathcal{R}_0$	$p$	$a$	$b$	$z_p$	$\Omega_{\text{ref}}$	$\alpha$
Joint search: Known SFR	$319^{+25}_{-24}$	$-1.00^{+0.04}_{-0.04}$	-	-	-	$1.92^{+0.58}_{-0.52} \times 10^{-11}$	$-0.10^{+0.32}_{-0.37}$
Joint search: Unknown SFR	$305^{+48}_{-47}$	-	$2.24^{+0.19}_{-0.16}$	$1.43^{+0.28}_{-0.24}$	$1.64^{+0.07}_{-0.07}$	$2.04^{+0.66}_{-0.66} \times 10^{-11}$	$-0.06^{+0.31}_{-0.39}$
Ideal search	-	-	-	-	-	$1.95^{+0.35}_{-0.34} \times 10^{-11}$	$-0.14^{+0.29}_{-0.31}$

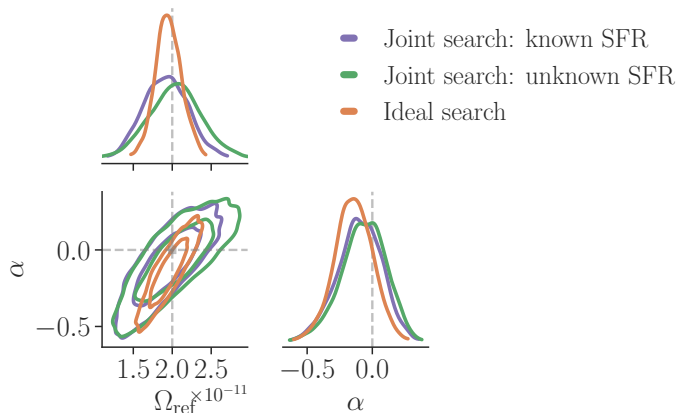


FIG. 2. Joint posterior distributions on  $\{\Omega_{\text{ref}}, \alpha\}$  across three different scenarios: known SFR (purple curves), unknown SFR (orange curves), and an ideal search without any CBC foreground (green curves). Contours represent 68% and 95% of the probability.

ence scheme, the recovery of the CGWB is not significantly affected by the presence of a CBC foreground. We find that the  $1\sigma$  error on the CGWB amplitude  $\Omega_{\text{ref}}$  increases by a factor of  $\sim 90\%$  ( $\sim 60\%$ ) in the unknown (known) SFR case compared to the ideal search with no foreground present. The difference in the marginalized posterior for the power-law index  $\alpha$  is even milder, with a 19% (17%) increase in the  $1\sigma$  error for the unknown (known) SFR scenario with respect to the ideal search.

**Sensitivity of the CGWB search.** In order to further assess the constraining power of our procedure, in Fig. 3 we compare the noise level for stochastic searches, the uncertainty on the BNS foreground, and the residual BBH foreground after notching out the resolved signals. The baseline noise level  $\sigma_n(f)$  is computed through Eqs. (S1) and (S2) of the Supplement. The uncertainty on the inferred BNS foreground is estimated by computing energy spectra  $\Omega_{\text{BNS}}(f)$  for all different posterior samples and the resulting standard deviation  $\sigma_{\Omega_{\text{BNS}}}(f)$  at each frequency (see the Supplement for the description of  $\Omega_{\text{BNS}}(f)$  calculation). The sensitivity of stochastic searches scales as  $\sim 1/\sqrt{T_{\text{obs}}}$  [51], so we show the comparison for different values of  $T_{\text{obs}}$  by simply rescaling  $\sigma_{\Omega_{\text{BNS}}}^{\text{rescaled}}(f) = \sigma_{\Omega_{\text{BNS}}}^{\text{obs}}(f) (\sqrt{T_{\text{obs}}}/\sqrt{T'_{\text{obs}}})$ . We also explicitly check this scaling by running the same full simulation using fewer data, in which case we do observe the width of the posterior distributions of parameters scale as  $1/\sqrt{T_{\text{obs}}}$

that further makes  $\sigma_{\Omega_{\text{BNS}}} \sim 1/\sqrt{T_{\text{obs}}}$ .

By only injecting BBHs signals into the time series and notching out the resolvable ones in the time-frequency domain as we did in Ref. [27, 28], we find that the residual BBH foreground is  $\sim 100$  times lower than the baseline noise  $\sigma_n(f)$  at every frequency, even for 10 yrs observation, which justifies neglecting its contribution to the joint likelihood in Eq. (4). The uncertainty on the BNS foreground differs by about 17% between the inference with known and unknown SFR, and it is well below the baseline noise at all frequencies, for both known and unknown SFR, and for all observation times. This is consistent with the results discussed in the previous section: the BNS foreground is well constrained in both our inferences, allowing us to decouple it from the CGWB. By applying the  $\sim 1/\sqrt{T_{\text{obs}}}$  scaling on the CGWB uncertainty, we can project sensitivity estimates for longer observations than 10 days. For the flat CGWB, we find that we can exclude  $\Omega_{\text{ref}} = 0$  at  $5\sigma$  level for  $\Omega_{\text{ref}} = 2.7 \times 10^{-12}/\sqrt{T_{\text{obs}}}$  ( $2.5 \times 10^{-12}/\sqrt{T_{\text{obs}}}$ ) in the unknown (known) SFR case, where  $T_{\text{obs}}$  is the observation time in years.

**Conclusions.** In this work, we combine the notching procedure of Refs. [27, 28] with the joint-likelihood approach of Ref. [34] to search for CGWBs with XG detectors. In this context, we demonstrate a methodology capable, for the first time, of simultaneously handling BBH signals, BNS signals, and a CGWB. Considering a simple population model for the hierarchical inference on the detected BNS events and a flat CGWB, we find that we can successfully claim detection of a sufficiently loud CGWB within 10 days of observation. In particular, for a flat CGWB with amplitude of  $\Omega_{\text{ref}} = 2.0 \times 10^{-11}$ , we find that we can exclude  $\Omega_{\text{ref}} = 0$  at at least  $\sim 6\sigma$  confidence level, depending on the assumptions on the BNS population model. The uncertainty on the recovered BNS foreground is well below the detector noise level. If we project the sensitivity to 1 year of observation, then we will reach the  $5\sigma$  sensitivity of  $\Omega_{\text{ref}} = 2.7 \times 10^{-12}$ , which is within a factor of  $\lesssim 2$  from the ideal stochastic search in absence of CBC foregrounds.

This study represents a crucial step forward in developing methods to detect CGWBs with XG detectors, but more work is needed before such methods can be applied to real data:

(1) We have assumed that the detector noise is perfectly known, while in practice, it can be challenging to estimate the PSD in the presence of glitches, non-stationary



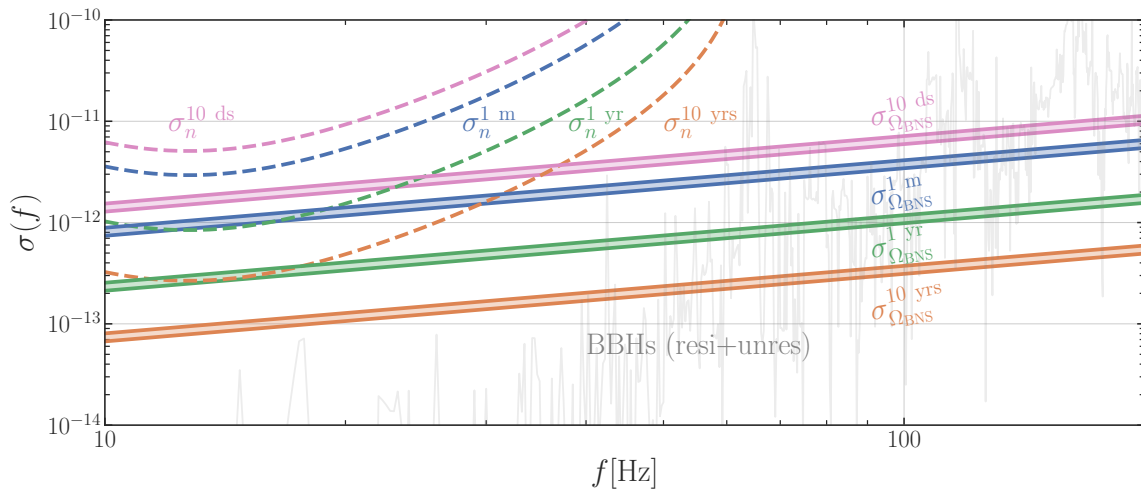


FIG. 3. The sensitivity of the CGWB search. The top four dashed curves show the baseline sensitivity to stochastic searches given different observation times: ten days (pink curve), one month (blue curve), one year (green curve), and ten years (orange curve). The straight bands represent the uncertainty on the BNS foreground for each observation time, with the same color scheme. Within each band, the upper (lower) line corresponds to the unknown (known) SFR scenario. The gray curve is the remaining BBH foreground after notching with 10 days of observation.

noise, cosmological and astrophysical SGWBs.

(2) We have neglected the contribution of NSBHs, which can give rise to an unresolved foreground that is comparable to the one from BNSs in XG detectors [29]. Our formalism can be straightforwardly extended to include a NSBH population. However, this would inevitably increase the computational cost and it could worsen the constraints on some of the inferred parameters.

(3) When performing hierarchical inference on the resolved BNS signals, we generate mock likelihood samples on the source parameters of individual events by using a Newtonian approximation of the signals and a Gaussian approximation of the likelihood [34, 50]. This method can underestimate errors on source parameters compared to performing full Bayesian PE with more realistic waveform models, although we still expect the population hyperparameters to be tightly constrained when the number of events is large enough [53]. Sampling individual-event likelihoods with full PE and state-of-the-art waveform models for several thousands of BNS signals in XG detectors is currently computationally prohibitive. Several promising techniques to speed up PE in preparation for XG detectors are being developed [54–57] and can be incorporated in our formalism in the future.

(4) We assume that the detected CBC signals originate from the same astrophysical population that generates the CBC foreground from unresolved signals. The presence of an unmodeled sub-population predominantly at high redshifts (e.g., from Population III stars [58] or primordial black holes [59]) could potentially give rise to biases in the estimate of the CBC foreground, and thus affect the detection of the CGWB.

We leave the exploration of these effects to future work.

**Acknowledgements** We thank Will M. Farr, Thomas Callister, and Francesco Iacovelli for helpful discussions. The authors are grateful for computational resources provided by the LIGO Laboratory and supported by National Science Foundation (NSF) Grants PHY-0757058 and PHY-0823459. B.Z. is supported by the Fermi Research Alliance, LLC, acting under Contract No. DE-AC02-07CH11359. E.B. and L.R. are supported by NSF Grants No. AST-2307146, PHY-2207502, PHY-090003 and PHY-20043, by NASA Grant No. 21-ATP21-0010, by the John Templeton Foundation Grant 62840, by the Simons Foundation, and by the Italian Ministry of Foreign Affairs and International Cooperation grant No. PGR01167. H.Z. and V.M. are in part supported by the NSF grant PHY-2409173. This work was carried out at the Advanced Research Computing at Hopkins (ARCH) core facility ([rockfish.jhu.edu](http://rockfish.jhu.edu)), which is supported by the NSF Grant No. OAC-1920103.

\* [zhong461@umn.edu](mailto:zhong461@umn.edu)

† [lreal1@jhu.edu](mailto:lreal1@jhu.edu)

‡ [beizhou@fnal.gov](mailto:beizhou@fnal.gov)

§ [berti@jhu.edu](mailto:berti@jhu.edu)

¶ [vuk@umn.edu](mailto:vuk@umn.edu)

- [1] D. Reitze, R. X. Adhikari, S. Ballmer, B. Barish, L. Barsotti, G. Billingsley, D. A. Brown, Y. Chen, D. Coyne, R. Eisenstein, *et al.*, [arXiv:1907.04833](https://arxiv.org/abs/1907.04833) (2019).
- [2] M. Evans, R. X. Adhikari, C. Afle, *et al.*, “A horizon study for cosmic explorer: Science, observatories, and community,” (2021).
- [3] V. Srivastava, D. Davis, K. Kuns, P. Landry, S. Ballmer, M. Evans, E. D. Hall, J. Read, and B. S. Sathyaprakash,

- Astrophys. J.* **931**, 22 (2022), arXiv:2201.10668 [gr-qc].
- [4] M. Punturo, M. Abernathy, F. Acernese, *et al.*, *Classical and Quantum Gravity* **27**, 194002 (2010).
- [5] M. Branchesi *et al.*, *JCAP* **07**, 068 (2023), arXiv:2303.15923 [gr-qc].
- [6] I. Gupta *et al.*, (2023), arXiv:2307.10421 [gr-qc].
- [7] M. Branchesi *et al.*, *JCAP* **07**, 068 (2023), arXiv:2303.15923 [gr-qc].
- [8] T. Regimbau, M. Evans, N. Christensen, E. Katsavounidis, B. Sathyaprakash, and S. Vitale, *Phys. Rev. Lett.* **118**, 151105 (2017).
- [9] A. I. Renzini, B. Goncharov, A. C. Jenkins, and P. M. Meyers, *Galaxies* **10**, 34 (2022), arXiv:2202.00178 [gr-qc].
- [10] L. P. Grishchuk, *Zh. Eksp. Teor. Fiz.* **67**, 825 (1974).
- [11] A. A. Starobinsky, *JETP Lett.* **30**, 682 (1979).
- [12] L. P. Grishchuk, *Phys. Rev. D* **48**, 3513 (1993), arXiv:gr-qc/9304018.
- [13] N. Barnaby, E. Pajer, and M. Peloso, *Phys. Rev. D* **85**, 023525 (2012), arXiv:1110.3327 [astro-ph.CO].
- [14] T. Damour and A. Vilenkin, *Phys. Rev. D* **71**, 063510 (2005), arXiv:hep-th/0410222.
- [15] X. Siemens, V. Mandic, and J. Creighton, *Phys. Rev. Lett.* **98**, 111101 (2007), arXiv:astro-ph/0610920.
- [16] S. Olmez, V. Mandic, and X. Siemens, *Phys. Rev. D* **81**, 104028 (2010), arXiv:1004.0890 [astro-ph.CO].
- [17] T. Regimbau, S. Giampanis, X. Siemens, and V. Mandic, *Phys. Rev. D* **85**, 066001 (2012), arXiv:1111.6638 [astro-ph.CO].
- [18] T. Callister, L. Sammut, S. Qiu, I. Mandel, and E. Thrane, *Phys. Rev. X* **6**, 031018 (2016), arXiv:1604.02513 [gr-qc].
- [19] S. Sachdev, T. Regimbau, and B. S. Sathyaprakash, *Phys. Rev. D* **102**, 024051 (2020).
- [20] B. Zhou, L. Reali, E. Berti, M. Çalıřkan, C. Creque-Sarbinowski, M. Kamionkowski, and B. S. Sathyaprakash, *Phys. Rev. D* **108**, 064040 (2023), arXiv:2209.01310 [gr-qc].
- [21] B. Zhou, L. Reali, E. Berti, M. Çalıřkan, C. Creque-Sarbinowski, M. Kamionkowski, and B. S. Sathyaprakash, arXiv (2022), arXiv:2209.01221 [gr-qc].
- [22] H. Song, D. Liang, Z. Wang, and L. Shao, arXiv (2024), arXiv:2401.00984 [gr-qc].
- [23] C. Cutler and J. Harms, *Phys. Rev. D* **73**, 042001 (2006), arXiv:gr-qc/0511092.
- [24] A. Sharma and J. Harms, *Phys. Rev. D* **102**, 063009 (2020), arXiv:2006.16116 [gr-qc].
- [25] Z. Pan and H. Yang, *Phys. Rev. D* **107**, 123036 (2023), arXiv:2301.04529 [gr-qc].
- [26] E. Belgacem, F. Iacovelli, M. Maggiore, M. Mancarella, and N. Muttoni, (2024), arXiv:2411.04029 [gr-qc].
- [27] H. Zhong, R. Ormiston, and V. Mandic, *Phys. Rev. D* **107**, 064048 (2023), [Erratum: *Phys. Rev. D* **108**, 089902 (2023)], arXiv:2209.11877 [gr-qc].
- [28] H. Zhong, B. Zhou, L. Reali, E. Berti, and V. Mandic, *Phys. Rev. D* **110**, 064047 (2024).
- [29] D. S. Bellie, S. Banagiri, Z. Doctor, and V. Kalogera, arXiv (2023), arXiv:2310.02517 [gr-qc].
- [30] R. Smith and E. Thrane, *Phys. Rev. X* **8**, 021019 (2018), arXiv:1712.00688 [gr-qc].
- [31] R. J. E. Smith, C. Talbot, F. Hernandez Vivanco, and E. Thrane, *Mon. Not. Roy. Astron. Soc.* **496**, 3281 (2020), arXiv:2004.09700 [astro-ph.HE].
- [32] S. Biscoveanu, C. Talbot, E. Thrane, and R. Smith, *Phys. Rev. Lett.* **125**, 241101 (2020), arXiv:2009.04418 [astro-ph.HE].
- [33] M. Li, J. Yu, and Z. Pan, arXiv (2024), arXiv:2403.01846 [gr-qc].
- [34] T. Callister, M. Fishbach, D. Holz, and W. Farr, *Astrophys. J. Lett.* **896**, L32 (2020), arXiv:2003.12152 [astro-ph.HE].
- [35] R. Abbott *et al.* (KAGRA, VIRGO, LIGO Scientific), *Phys. Rev. X* **13**, 011048 (2023), arXiv:2111.03634 [astro-ph.HE].
- [36] P. Landry and J. S. Read, *Astrophys. J. Lett.* **921**, L25 (2021), arXiv:2107.04559 [astro-ph.HE].
- [37] B. Finkel, H. Andresen, and V. Mandic, *Phys. Rev. D* **105**, 063022 (2022), arXiv:2110.01478 [gr-qc].
- [38] J. Aasi *et al.* (LIGO Scientific), *Class. Quant. Grav.* **32**, 074001 (2015), arXiv:1411.4547 [gr-qc].
- [39] F. Acernese *et al.* (VIRGO), *Class. Quant. Grav.* **32**, 024001 (2015), arXiv:1408.3978 [gr-qc].
- [40] G. Ashton, M. Hübner, P. D. Lasky, C. Talbot, K. Ackley, S. Biscoveanu, Q. Chu, A. Divakarla, P. J. Easter, B. Goncharov, *et al.*, *The Astrophysical Journal Supplement Series* **241**, 27 (2019).
- [41] G. Pratten, S. Husa, C. García-Quirós, M. Colleoni, A. Ramos-Buades, H. Estellés, and R. Jaume, *Phys. Rev. D* **102**, 064001 (2020).
- [42] A. Buonanno, Y.-b. Chen, and M. Vallisneri, *Phys. Rev. D* **67**, 104025 (2003), [Erratum: *Phys. Rev. D* **74**, 029904 (2006)], arXiv:gr-qc/0211087.
- [43] A. I. Renzini, A. Romero-Rodríguez, C. Talbot, *et al.*, *The Astrophysical Journal* **952**, 25 (2023).
- [44] B. S. Sathyaprakash and B. F. Schutz, *Living Rev. Rel.* **12**, 2 (2009), arXiv:0903.0338 [gr-qc].
- [45] I. Mandel, W. M. Farr, and J. R. Gair, *Mon. Not. Roy. Astron. Soc.* **486**, 1086 (2019), arXiv:1809.02063 [physics.data-an].
- [46] S. R. Taylor and D. Gerosa, *Phys. Rev. D* **98**, 083017 (2018), arXiv:1806.08365 [astro-ph.HE].
- [47] V. Mandic, E. Thrane, S. Giampanis, and T. Regimbau, *Phys. Rev. Lett.* **109**, 171102 (2012), arXiv:1209.3847 [astro-ph.CO].
- [48] T. Callister, A. S. Biscoveanu, N. Christensen, M. Isi, A. Matas, O. Minazzoli, T. Regimbau, M. Sakellariadou, J. Tasson, and E. Thrane, *Phys. Rev. X* **7**, 041058 (2017), arXiv:1704.08373 [gr-qc].
- [49] K. K. Y. Ng, S. Vitale, W. M. Farr, and C. L. Rodriguez, *Astrophys. J. Lett.* **913**, L5 (2021), arXiv:2012.09876 [astro-ph.CO].
- [50] M. Fishbach, D. E. Holz, and W. M. Farr, *Astrophys. J. Lett.* **863**, L41 (2018), arXiv:1805.10270 [astro-ph.HE].
- [51] B. Allen and J. D. Romano, *Phys. Rev. D* **59**, 102001 (1999), arXiv:gr-qc/9710117.
- [52] R. Abbott *et al.* (LIGO Scientific Collaboration, Virgo Collaboration, and KAGRA Collaboration), *Phys. Rev. D* **104**, 022004 (2021).
- [53] V. De Renzi, F. Iacovelli, D. Gerosa, M. Mancarella, and C. Pacilio, (2024), arXiv:2410.17325 [astro-ph.HE].
- [54] S. R. Green and J. Gair, *Mach. Learn. Sci. Tech.* **2**, 03LT01 (2021), arXiv:2008.03312 [astro-ph.IM].
- [55] M. Dax, S. R. Green, J. Gair, M. Pürrer, J. Wildberger, J. H. Macke, A. Buonanno, and B. Schölkopf, *Phys. Rev. Lett.* **130**, 171403 (2023), arXiv:2210.05686 [gr-qc].
- [56] K. W. K. Wong, M. Isi, and T. D. P. Edwards, *Astrophys. J.* **958**, 129 (2023), arXiv:2302.05333 [astro-ph.IM].
- [57] J. Alvey, U. Bhardwaj, S. Nissanke, and C. Weniger, (2023), arXiv:2308.06318 [gr-qc].

- [58] K. Martinovic, C. Perigois, T. Regimbau, and M. Sakellariadou, *Astrophys. J.* **940**, 29 (2022), arXiv:2109.09779 [astro-ph.SR].
- [59] S. Mukherjee, M. S. P. Meinema, and J. Silk, *Mon. Not. Roy. Astron. Soc.* **510**, 6218 (2022), arXiv:2107.02181 [astro-ph.CO].

# Supplemental Material: A Two-Step Procedure to Detect Cosmological Gravitational Wave Backgrounds with Next-Generation Terrestrial Gravitational-Wave Detectors

## I. NOTCHING PROCEDURE

In this section, we define the cross-correlation statistics we adopt for the stochastic search and briefly outline the notching procedure of Ref. [S1], which we use to remove all the detected binary black hole (BBH) signals from data.

### A. Stochastic search

Let us consider two gravitational wave (GW) detectors  $I, J$  with strain time series  $h_I(t), h_J(t)$ . To perform the cross-correlation search for the stochastic gravitational wave background (SGWB), we split the strains into time segments  $t_i$  of duration  $T = 4$  s. For each frequency bin  $f_j$ , we denote the Fourier transforms of these segments by  $\tilde{h}_{I,J}(t_i; f_j)$  and their complex conjugates with an asterisk. For the baseline of these two detectors, one can define the cross-correlation statistics  $\hat{C}_{IJ}(t_i; f_j)$  and the corresponding variance estimator  $\hat{\sigma}_{IJ}^2$  as [S2, S3]

$$\begin{aligned}\hat{C}_{IJ}(t_i; f_j) &= \left( \frac{20\pi^2 f_j^3}{3H_0^2 T} \right) \frac{\text{Re}[\tilde{h}_I^*(t_i; f_j)\tilde{h}_J(t_i; f_j)]}{\gamma_{IJ}(f_j)}, \\ \hat{\sigma}_{IJ}^2(t_i; f_j) &= \left( \frac{20\pi^2 f_j^3}{3H_0^2} \right)^2 \frac{P_{n_I}(t_i; f_j)P_{n_J}(t_i; f_j)}{8T\Delta f \gamma_{IJ}^2(f_j)}.\end{aligned}\quad (\text{S1})$$

Here  $\gamma_{IJ}(f_j)$  is the overlap reduction function between the two detectors [S3],  $\Delta f = 0.25$  Hz is the Fourier transform resolution,  $P_{n_I}(t_i; f_j)$  is the power spectral density (PSD) of the  $I$ th detector at time  $t_i$ , and  $H_0$  is the Hubble constant. The time-averaged frequency-domain spectrum  $\hat{C}_{IJ}(f_j)$  and its variance  $\hat{\sigma}_{IJ}^2(f_j)$  can then be obtained by performing a weighted average over all time segments:

$$\begin{aligned}\hat{C}_{IJ}(f_j) &= \frac{\sum_i \hat{C}_{IJ}(t_i; f_j) \hat{\sigma}_{IJ}^{-2}(t_i; f_j)}{\sum_i \hat{\sigma}_{IJ}^{-2}(t_i; f_j)}, \\ \hat{\sigma}_{IJ}^{-2}(f_j) &= \sum_i \frac{1}{\hat{\sigma}_{IJ}^2(t_i; f_j)}.\end{aligned}\quad (\text{S2})$$

With a network of more than two detectors, these spectra can be further combined by computing weighted averages among all the possible detector pairs. As mentioned in the main text however, in this study we perform the cross-correlation search using only a baseline of two CE detectors, since including all the other possible baselines would only lead to a  $\lesssim 10\%$  improvement [S1]. Throughout this work, we denote the frequency domain cross-correlation spectrum and its variance from this baseline *before notching* with  $\hat{C}(f)$  and  $\sigma^2(f)$ , respectively.

### B. Mask definition

We notch out all the resolved BBH signals in our dataset by applying the time-frequency approach of Ref. [S1]. We consider a signal  $h$  to be individually resolved if its network signal-to-noise ratio (SNR)

$$\rho = \sqrt{\sum_{J=1}^{N_{\text{det}}} (h)_J} \quad (\text{S3})$$

is above a certain threshold, where  $(\cdot|\cdot)$  denotes the usual signal inner product

$$(a|b) = 4 \text{Re} \int_0^\infty \frac{a(f)b^*(f)}{P_n(f)} df, \quad (\text{S4})$$



and the sum index  $J$  runs over all the  $N_{\text{det}}$  detectors in the network. For BBHs, we choose a detection threshold of  $\rho_{\text{thr}}^{\text{BBH}} = 8$  [S1]. We estimate the impact of the imperfect recovery of the signals on the notching procedure via their Fisher matrix [S4]

$$\Gamma_{\alpha\beta} = \sum_{J=1}^{N_{\text{det}}} \left( \frac{\partial h}{\partial \theta^\alpha} \middle| \frac{\partial h}{\partial \theta^\beta} \right)_J, \quad (\text{S5})$$

with  $\theta^\alpha$  denoting the source parameters. We consider a set of 9 parameters ignoring spin of all compact binary coalescences (CBCs)

$$\boldsymbol{\theta} = \left\{ \ln \left( \frac{\mathcal{M}_z^c}{M_\odot} \right), \eta, \ln \left( \frac{d_L}{\text{Mpc}} \right), \cos \iota, \cos \delta, \alpha, \psi, \phi_c, t_c \right\}. \quad (\text{S6})$$

Here,  $\mathcal{M}_z^c = \mathcal{M}_c(1+z)$  is the detector-frame chirp mass, with  $\mathcal{M}_c = (m_1 m_2)^{3/5} / (m_1 + m_2)^{1/5}$ , and  $m_{1,2}$  the component masses;  $\eta = (m_1 m_2) / (m_1 + m_2)^2$  is the symmetric mass ratio;  $d_L$  is the luminosity distance;  $\iota, \psi$  are the inclination and polarization angles;  $\alpha, \delta$  are the right ascension and declination angles;  $\phi_c, t_c$  are the phase and time of coalescence. We compute the Fisher matrices with the public package **GWBENCH** [S5].

For each detected BBH event ( $\rho^{\text{BBH}} > 8$ ), we sample its source parameters from a multivariate normal distribution  $\mathcal{N}(\hat{\boldsymbol{\theta}}, \Gamma^{-1})$ , with mean located at the true values of the parameters  $\hat{\boldsymbol{\theta}}$ . We determine the mask in the time-frequency domain on zero-noise data containing these sampled signals only. We use Eqs. (S1) to define SNR maps as

$$\text{SNR}_{\text{IJ}}(t_i; f_j) = \left| \hat{C}_{\text{IJ}}(t_i; f_j) / \hat{\sigma}_{\text{IJ}}(t_i; f_j) \right|. \quad (\text{S7})$$

We adopt an SNR threshold of  $5 \times 10^{-4}$  to identify the tracks associated to the signals [S1, S6]. Our mask comprises all the pixels that pass this threshold. Given these masks, we can notch out CBC tracks. We denote the cross-correlation spectra and the detector noise after notching by  $\hat{C}^*(f)$  and  $(\sigma^*)^2(f)$ , respectively.

## II. JOINT INFERENCE METHOD

After removing all the resolved BBH signals, we perform joint Bayesian inference on the remaining data, which contain binary neutron star (BNS) signals, the cosmological gravitational wave background (CGWB), and the notching residual. In this section, we provide details on the calculation of the joint likelihood we use for the inference.

### A. Joint likelihood

Let us consider a BNS population characterized by hyperparameters  $\boldsymbol{\Lambda}_{\text{BNS}}$  and a CGWB with parameters  $\boldsymbol{\Lambda}_{\text{CGWB}}$ . The joint likelihood for the individual BNS detections  $\{\mathbf{d}_i\}_{i=1}^{N_{\text{obs}}}$  and the SGWB cross-correlation spectrum  $C^*(f)$  can be factorized as [S7]

$$\mathcal{L}(\{\mathbf{d}_i\}_{i=1}^{N_{\text{obs}}}, \hat{C}^*(f) | \boldsymbol{\Lambda}_{\text{BNS}}, \boldsymbol{\Lambda}_{\text{CGWB}}) = \mathcal{L}_{\text{BNS}}(\{\mathbf{d}_i\}_{i=1}^{N_{\text{obs}}} | \boldsymbol{\Lambda}_{\text{BNS}}) \times \mathcal{L}_{\text{SGWB}}(\hat{C}^*(f) | \boldsymbol{\Lambda}_{\text{BNS}}, \boldsymbol{\Lambda}_{\text{CGWB}}). \quad (\text{S8})$$

The first term on the right-hand side is the usual hierarchical likelihood for population inference with individually resolved signals [S8, S9]

$$\mathcal{L}(\{\mathbf{d}_i\}_{i=1}^{N_{\text{obs}}} | \boldsymbol{\Lambda}_{\text{BNS}}) \propto [N(\boldsymbol{\Lambda}_{\text{BNS}}) \xi(\boldsymbol{\Lambda}_{\text{BNS}})]^{N_{\text{obs}}} e^{-N(\boldsymbol{\Lambda}_{\text{BNS}}) \xi(\boldsymbol{\Lambda}_{\text{BNS}})} \left[ \prod_{i=1}^{N_{\text{obs}}} \frac{\int d\boldsymbol{\theta} p(\mathbf{d}_i | \boldsymbol{\theta}) p_{\text{pop}}(\boldsymbol{\theta} | \boldsymbol{\Lambda}_{\text{BNS}})}{\xi(\boldsymbol{\Lambda}_{\text{BNS}})} \right]. \quad (\text{S9})$$

Here,  $p(\mathbf{d}_i | \boldsymbol{\theta})$  is the likelihood for the individually detected event  $i$  given the source parameters  $\boldsymbol{\theta}$ ;  $p_{\text{pop}}(\boldsymbol{\theta} | \boldsymbol{\Lambda}_{\text{BNS}})$  is the ensemble distribution of the source parameters given population hyperparameters  $\boldsymbol{\Lambda}_{\text{BNS}}$ ;  $N_{\text{obs}}$  is the number of events actually detected; and  $\xi(\boldsymbol{\Lambda}_{\text{BNS}})$  is the expected fraction of resolvable events, given a population model with hyperparameters  $\boldsymbol{\Lambda}_{\text{BNS}}$ . We highlight that in this work, we treat *detectable* and *resolvable* as synonymous and use the terms interchangeably.

If the probability of detecting a signal with source parameters  $\boldsymbol{\theta}$  is  $p_{\text{det}}(\boldsymbol{\theta})$ , the fraction  $\xi(\boldsymbol{\Lambda}_{\text{BNS}})$  is given by

$$\xi(\boldsymbol{\Lambda}_{\text{BNS}}) = \int p_{\text{det}}(\boldsymbol{\theta}) p_{\text{pop}}(\boldsymbol{\theta} | \boldsymbol{\Lambda}_{\text{BNS}}) d\boldsymbol{\theta}. \quad (\text{S10})$$

We compute  $p_{\text{det}}(\boldsymbol{\theta})$  on a grid of masses and redshifts with a hard SNR cutoff. For BNSs, we choose a detection SNR threshold of  $\rho_{\text{thr}}^{\text{BNS}} = 12$  [S1]. The expected total number of events (both resolved and unresolved) given population hyperparameters  $\boldsymbol{\Lambda}_{\text{BNS}}$ ,  $N(\boldsymbol{\Lambda}_{\text{BNS}})$ , can be calculated as follows:

$$N(\boldsymbol{\Lambda}_{\text{BNS}}) = T_{\text{obs}} \int_0^{z_{\text{max}}} dz \frac{1}{1+z} \mathcal{R}_m(z|\boldsymbol{\Lambda}_{\text{BNS}}) \left. \frac{dV_c}{dz} \right|_z, \quad (\text{S11})$$

where  $T_{\text{obs}}$  is the observation time,  $\mathcal{R}_m(z|\boldsymbol{\Lambda}_{\text{BNS}})$  is the source-frame merger rate per unit comoving volume, and  $dV_c/dz$  is the comoving volume element per redshift slice  $dz$ .

Regarding the BNS population model  $p_{\text{pop}}(\boldsymbol{\theta}|\boldsymbol{\Lambda}_{\text{BNS}})$ , we assume that all of the angular parameters are isotropically distributed and that the mass distribution is uniform, redshift-independent, and perfectly known. In other words, the only hyperparameters left to determine are the ones characterizing the redshift distribution

$$p_{\text{pop}}(\boldsymbol{\theta}|\boldsymbol{\Lambda}_{\text{BNS}}) \propto p(z|\boldsymbol{\Lambda}_{\text{BNS}}). \quad (\text{S12})$$

The second term on the right-hand side of Eq. (S8) is the usual Gaussian likelihood for the SGWB cross-correlation spectrum [S10, S11]

$$\mathcal{L}_{\text{SGWB}}(\hat{C}^*(f)|\boldsymbol{\Lambda}_{\text{BNS}}, \boldsymbol{\Lambda}_{\text{CGWB}}) \propto \prod_i \exp\left(-\frac{[\hat{C}^*(f_i) - \Omega_{\text{SGWB}}(f_i; \boldsymbol{\Lambda}_{\text{BNS}}, \boldsymbol{\Lambda}_{\text{CGWB}})]^2}{2(\sigma^*)^2(f_i)}\right), \quad (\text{S13})$$

where  $\Omega_{\text{SGWB}}(f)$  is the expected energy density spectrum of the total SGWB, and the product is over all frequency bins  $f_i$ . After notching out all the resolved BBH signals, the expected energy density of the total SGWB consists of four contributions:

$$\Omega_{\text{SGWB}}(f) = \Omega_{\text{BNS}}(f|\boldsymbol{\Lambda}_{\text{BNS}}) + \Omega_{\text{CGWB}}(f|\boldsymbol{\Lambda}_{\text{CGWB}}) + \Omega_{\text{BBH,resi}}(f) + \Omega_{\text{BBH,unres}}(f). \quad (\text{S14})$$

Here  $\Omega_{\text{BNS}}(f)$  is the foreground generated by all BNS events (both resolved and unresolved),  $\Omega_{\text{CGWB}}(f)$  is the cosmological background,  $\Omega_{\text{BBH,resi}}(f)$  is the residual foreground after notching out the resolved BBH signals, and  $\Omega_{\text{BBH,unres}}(f)$  is the foreground from the few unresolvable BBH signals. We find that the BBH contribution  $\Omega_{\text{BBH,resi}}(f) + \Omega_{\text{BBH,unres}}(f)$  after notching is well below noise level (see Fig. 4 of the main text). For this reason we neglect it in our inference, and we only take  $\Omega_{\text{BNS}}(f|\boldsymbol{\Lambda}_{\text{BNS}})$  and  $\Omega_{\text{CGWB}}(f|\boldsymbol{\Lambda}_{\text{CGWB}})$  into account. The expected BNS foreground is given by [S12]

$$\Omega_{\text{BNS}}(f|\boldsymbol{\Lambda}_{\text{BNS}}) = \frac{f}{\rho_c H_0} \int_0^{z_{\text{max}}} dz \frac{\mathcal{R}_m(z|\boldsymbol{\Lambda}_{\text{BNS}})}{(1+z)E(z)} \left\langle \frac{dE}{df} \right\rangle_{f(1+z)} \Big|_{\boldsymbol{\Lambda}_{\text{BNS}}}. \quad (\text{S15})$$

Here,  $\rho_c$  is the critical energy density required to close the universe;  $E(z) = \sqrt{\Omega_\Lambda + (1+z)^3 \Omega_M}$  is the Hubble parameter at redshift  $z$  neglecting radiation density, where we take the energy densities of matter and dark energy to be  $\Omega_M = 0.3$  and  $\Omega_\Lambda = 0.7$ , respectively; and  $\langle dE/df \rangle_{\boldsymbol{\Lambda}_{\text{BNS}}}$  is the expectation value over the BNS population of the source-frame energy spectrum radiated by a single BNS source. We estimate  $dE/df$  via the Newtonian approximation [S12]

$$\left\langle \frac{dE}{df} \right\rangle_{f(1+z)} \Big|_{\boldsymbol{\Lambda}_{\text{BNS}}} = \frac{(\pi G)^{2/3} \langle \mathcal{M}_c \rangle_{\boldsymbol{\Lambda}_{\text{BNS}}}^{5/3}}{3} [f(1+z)]^{-1/3}, \quad (\text{S16})$$

where  $G$  is the gravitational constant, and  $\langle \mathcal{M}_c \rangle_{\boldsymbol{\Lambda}_{\text{BNS}}}$  is the expectation value of the source-frame chirp mass over the BNS population.

For the expected CGWB, we instead consider a power-law background

$$\Omega_{\text{CGWB}}(f|\boldsymbol{\Lambda}_{\text{CGWB}}) = \Omega_{\text{ref}} \left( \frac{f}{f_{\text{ref}}} \right)^\alpha, \quad (\text{S17})$$

where  $\boldsymbol{\Lambda}_{\text{CGWB}} = \{\Omega_{\text{ref}}, \alpha\}$ . In our simulations, we will assume  $\alpha = 0$  and  $\Omega_{\text{ref}} = 2 \times 10^{-11}$  at  $f_{\text{ref}} = 25$  Hz.

## B. Mock likelihoods for resolved BNSs

For each detected BNS event ( $\rho^{\text{BNS}} > 12$ ), the integral in the hierarchical likelihood of Eq. (S9) can be approximated as an average over discrete likelihood samples

$$\int d\boldsymbol{\theta} p(\boldsymbol{d}_i|\boldsymbol{\theta}) p_{\text{pop}}(\boldsymbol{\theta}|\boldsymbol{\Lambda}_{\text{BNS}}) \approx \left\langle p_{\text{pop}}(\boldsymbol{\theta}_i|\boldsymbol{\Lambda}_{\text{BNS}}) \right\rangle_{\text{Likelihood samples}}. \quad (\text{S18})$$

In a real inference, one typically has access to samples drawn from the individual events' posterior distributions  $p(\boldsymbol{\theta}|\mathbf{d}_i)$ , which then need to be reweighted by the adopted parameter estimation (PE) prior  $p(\boldsymbol{\theta})$  to obtain the likelihood samples. Performing full Bayesian PE for thousands of BNS events in next generation (XG) detectors is, however, currently computationally unfeasible. Hence, we generate synthetic likelihood samples for each detected event following a procedure similar to Refs. [S7, S13].

Given our assumptions on the BNS population model (see Eq. (S11)), for each detected event, we only need to generate mock likelihood samples on the redshift  $z$ . The redshift (or rather, the luminosity distance  $d_L$ ) is mainly determined by the waveform amplitude. For BNS signals, the polarization amplitudes  $A_+$  and  $A_\times$  can be well described by the Newtonian approximation [S14]

$$\begin{aligned} A_+(\mathcal{M}_c^z, d_L, \cos \iota) &= \sqrt{\frac{5}{24}} \frac{(G\mathcal{M}_c^z)^{5/6}}{2\pi^{2/3}c^{3/2}d_L} (1 + \cos^2 \iota), \\ A_\times(\mathcal{M}_c^z, d_L, \cos \iota) &= \sqrt{\frac{5}{24}} \frac{(G\mathcal{M}_c^z)^{5/6}}{\pi^{2/3}c^{3/2}d_L} \cos \iota. \end{aligned} \quad (\text{S19})$$

The resulting strain amplitude is thus

$$A(\mathcal{M}_c^z, d_L, \cos \iota) = \sqrt{A_\times^2 + A_+^2} = \frac{\mathcal{K}^2 \mathcal{M}_c^{z,5/3}}{4d_L^2} \mathcal{F}(\cos \iota), \quad (\text{S20})$$

where  $\mathcal{K}$  encodes all the constants and

$$\mathcal{F}(\cos \iota) = \sqrt{(1 + \cos^2 \iota)^2 + 4 \cos^2 \iota}. \quad (\text{S21})$$

For each resolved BNS, we draw likelihood samples for the strain amplitude  $A$  from a Gaussian distribution

$$\{A\} \sim \mathcal{N}(\bar{A}, \sigma_A), \quad (\text{S22})$$

where  $\bar{A}$  is the true value determined via the injected parameters. In this formalism,  $\sigma_A$  represents the detector noise level, and the ratio  $\rho^* = \bar{A}/\sigma_A$  is a proxy for SNR. We fix the value  $\sigma_A = 1.09 \times 10^{-24}$  such that the number of signals that satisfy  $\rho^* \geq \rho_{\text{thr}}^{\text{BNS}} = 12$  in this approximation matches the number of resolved BNS signals in our pipeline. We then draw likelihood samples for the detector-frame chirp mass  $\mathcal{M}_c^z$  and the factor  $\mathcal{F}(\cos \iota)$  from Gaussian distributions centered at the injected values  $\bar{\mathcal{M}}_c^z, \bar{\mathcal{F}}(\cos \iota)$ :

$$\{\mathcal{M}_c^z\} \sim \mathcal{N}\left(\bar{\mathcal{M}}_c^z, \sigma_{\mathcal{M}} \frac{12}{\rho^*}\right), \quad \{\mathcal{F}(\cos \iota)\} \sim \mathcal{N}\left(\bar{\mathcal{F}}(\cos \iota), \sigma_{\mathcal{F}} \frac{12}{\rho^*}\right). \quad (\text{S23})$$

The values of  $\sigma_{\mathcal{M}}$  and  $\sigma_{\mathcal{F}}$  are derived from Ref. [S7]. In their work, they provide a reference error  $\sigma_{\Theta} = 0.15$  for the projection factor [S15]

$$\Theta = 4\sqrt{\frac{F_+^2(\alpha, \delta, \psi)}{4}(1 + \cos^2 \iota)^2 + F_\times^2(\alpha, \delta, \psi) \cos^2 \iota}, \quad (\text{S24})$$

where  $F_{+,\times}(\alpha, \delta, \psi)$  are the antenna patterns of a given GW detector. By fixing  $F_+$  and  $F_\times$  to their sky-averaged values  $\langle F_+^2 \rangle_{\text{sky}} = \langle F_\times^2 \rangle_{\text{sky}} = 1/5$  [S14] and comparing with Eq. (S21), we obtain

$$\sigma_{\mathcal{F}} \approx \frac{\sqrt{5}}{2} \sigma_{\Theta} = 0.167. \quad (\text{S25})$$

Regarding the chirp mass, Ref. [S7] provides a value of  $\sigma_{\mathcal{M}} = 0.08 M_\odot$  for BBHs. Since in this work we apply the formalism to BNS signals, we empirically scale this value to  $\sigma_{\mathcal{M}} = 0.01 M_\odot$ . We check the validity of this approximation in the next section.

Given likelihood samples for  $A$ ,  $\mathcal{M}_c^z$  and  $\mathcal{F}(\cos \iota)$ , we finally obtain likelihood samples for  $d_L$  by inverting Eq. (S20), and we convert them into redshift samples assuming the Planck 2018  $\Lambda$ CDM cosmological model [S16]. Albeit simplistic, this method allows us to capture some of the key correlations that drive the uncertainty on the redshift, namely SNR, inclination, and chirp mass [S7].

### C. Comparison with Fisher matrix

As an alternative, one could generate mock likelihood samples for individually resolved BNSs via the Fisher approximation [S4]. For instance, this is the approach we used to estimate errors on BBH source parameters in the notching procedure (see Sec. IB). However, the approximation is strictly valid only in the high-SNR regime, and a large fraction of the resolved BNS signals have SNR barely above the detection threshold. Furthermore, several events are expected to produce ill-conditioned Fisher matrices [S17], which are notoriously unreliable to invert and can significantly mispredict the likelihood [S18]. While these effects do not cause significant issues in the notching procedure [S1], they can significantly impact the estimate of the error on luminosity distance (and thus redshift) [S19].

For these reasons, and given the demonstrative purpose of this work, we choose to generate mock likelihood samples with the approach described in the previous Section.

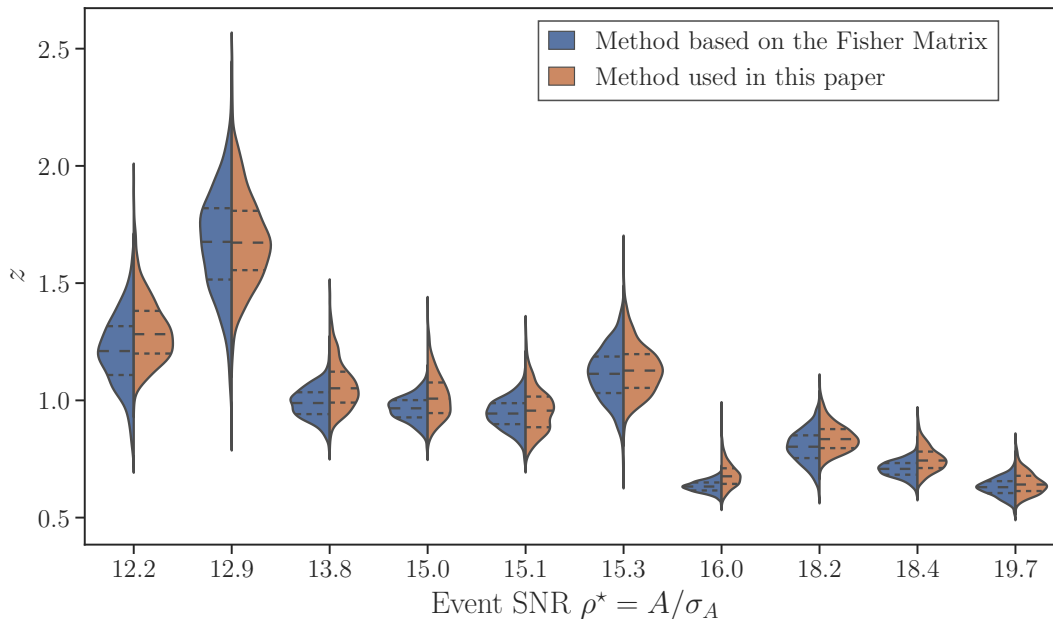


FIG. S1. Comparison between mock likelihoods on redshift obtained either via Fisher matrix (blue distributions) or via the approach of Sec. IIB (orange distributions). Results are shown for several low-SNR BNS events and with well-conditioned Fisher matrices drawn from our population. Dashed lines indicate 25%, 50%, and 75% quantiles.

In Fig. S1, we compare mock likelihood redshift samples generated with a Fisher-matrix approximation and with the approach described in Sec. IIB. We show results for several BNS events with low effective SNR  $\rho^*$  (which are expected to provide the dominant contribution to the uncertainty in the population inference) and well-conditioned Fisher matrices. The Fisher matrices are generated with the public package `GWfish` [S20] considering all nine parameters listed in the Eq. (S6) and `IMRphenomXAS` waveform model. The estimated marginalized likelihoods with the two methods are in good agreement for all the events shown, validating the robustness of our approach.

In an actual inference, one would need to perform full Bayesian PE on all the resolved BNS events, which is currently computationally unfeasible in the context of XG detectors. In practice, we expect that considering more realistic waveform models with more parameters compared to Eqs. (S19) and performing full PE would lead to wider redshift likelihoods compared to our approach. This is due both to the correlations introduced by the additional parameters, and to the potentially non-Gaussian nature of the likelihoods for low-SNR events. In this sense, our results represent an optimistic forecast of the capability of our framework in the context of XG detectors. However, we argue that the analysis performed in this work only makes use of 10 days of data, and tight constraints on the population parameters can always be achieved by stacking a larger number of events together. Several promising methods to accelerate PE in preparation for XG detectors are being developed (see e.g. [S21–S25]) and can potentially be incorporated in our framework in the future.

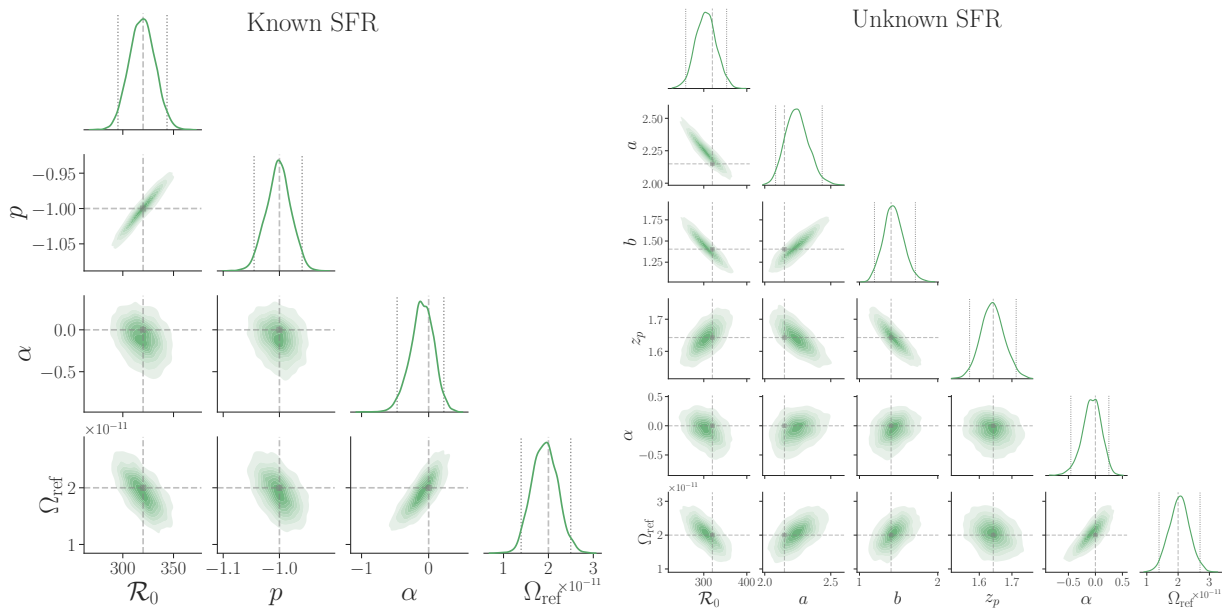


FIG. S2. Inferred posterior distributions on the BNS hyperparameters and the CGWB parameters for the scenarios with known (left corner plot) and unknown (right corner plot) SFR. The gray dashed lines indicate the injected values, while the gray dotted lines show the 95% credible intervals in the marginalized 1D posterior distributions.

### III. ADDITIONAL RESULTS

In this section, we provide more details on the results of our joint inference and compare them with the constraints one would obtain from (i) individual BNS detections only, or (ii) the SGWB search only.

#### A. Joint inference results

TABLE I. Priors placed on the hyperparameters describing the BNS merger rate and population and the CGWB.

Parameter	Prior	Minimum	Maximum
$\mathcal{R}_0$	Log-uniform	10	1700
$p$	Uniform	-3	0
$a$	Uniform	0	10
$b$	Uniform	0	10
$z_p$	Uniform	0	4
$\Omega_{\text{ref}}$	Log-uniform	$10^{-15}$	$10^{-10}$
$\alpha$	Uniform	-3	3

In Fig. S2, we show the posterior distributions on all the parameters of our joint inference for both scenarios we consider. The priors we impose are listed in Table I. As discussed in the main text, we find that the CGWB parameters are well constrained in both cases, allowing us to exclude a  $\Omega_{\text{ref}} = 0$  amplitude at least  $6\sigma$  level. With only 10 days of observation, corresponding to roughly  $\sim 7000$  detections of individual BNS events, we find that the hyperparameters of the BNS redshift distribution are also well constrained. The 95% errors on all the parameters describing the shape of the merger rate are of order  $\sim 10\%$  or less. The median and 95% credible interval of the posterior distributions of all parameters are shown in Table I of the main text.

The constraints on the source-frame BNS merger rate as a function of redshift are shown in Fig. S3. The grey curves are obtained with different posterior samples on the BNS hyperparameters, namely  $\{\mathcal{R}_0, p\}$  ( $\{\mathcal{R}_0, a, b, z_p\}$ ) in the case with known (unknown) SFR. Assuming prior knowledge of the SFR, and thus including fewer parameters in the inference, allows for more stringent constraints in  $R_m(z)$  in all redshift bins. This effect is particularly prominent at redshifts  $z \gtrsim 3$ , where less BNS detections are available. In particular, we show the ratio of the standard deviations



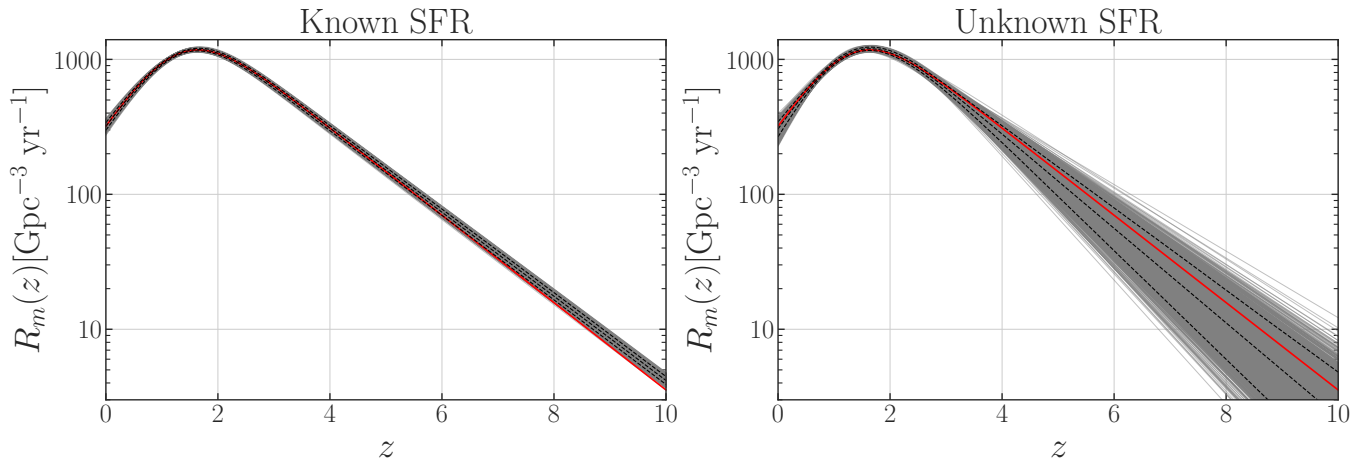


FIG. S3. Inferred source-frame BNS merger rate  $R_m(z)$  as a function of redshift in the two scenarios we consider. Each gray curve corresponds to the merger rate obtained with a different posterior sample on BNS hyperparameters. The three dashed black curves denote the median and 90% quantiles. The red curve depicts the injected  $R_m(z)$ .

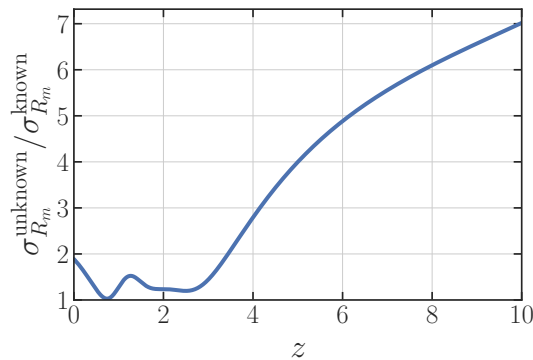


FIG. S4. Ratio of the standard deviation in the inferred BNS merger rate  $R_m(z)$  as a function of redshift between the unknown SFR and the known SFR cases.

in the inferred merger rate between the two cases in Fig. S4. The standard deviation in the unknown SFR case is larger by a factor of  $\lesssim 2$  at low redshifts, and then starts increasing monotonically at  $z \gtrsim 3$ .

In Fig. S5, we show the inferred energy spectra  $\Omega_{\text{GW}}(f)$  for both the BNS foreground and the CGWB using Eq. (S15) to Eq. (S17). We find that the BNS foreground spectrum can be tightly constrained in both scenarios we consider. The uncertainty on the BNS foreground is larger in the more realistic case with unknown SFR, reflecting the larger uncertainty on the merger rate shown in Fig. S3. In particular, we find that the standard deviation on  $\Omega_{\text{GW}}(f)$  is roughly  $\sim 20\%$  smaller in every frequency bin in the case with known SFR, namely  $\sigma_{\text{BNS}}^{\text{Known SFR}}(f) = 0.83 \sigma_{\text{BNS}}^{\text{Unknown SFR}}(f)$ . The recovered CGWB is remarkably similar in both cases, reflecting the similarity in the joint posterior distribution of  $(\Omega_{\text{ref}}, \alpha)$ . Constraints get significantly worse at higher frequencies, as the baseline sensitivity to stochastic searches decreases.

## B. Joint inference vs individual BNS only

In Fig. S6, we compare the posterior distributions on BNS hyperparameters from the joint inference with the posteriors resulting only from the hierarchical inference on the individually detected BNS signals. In other words, we compare inference results obtained from the full joint likelihood  $\mathcal{L}(\{\mathbf{d}_i\}_{i=1}^{N_{\text{obs}}}, \hat{C}^*(f) | \mathbf{\Lambda}_{\text{BNS}}, \mathbf{\Lambda}_{\text{CGWB}})$  of Eq. (S8) with results obtained from just the first term of the same equation,  $\mathcal{L}_{\text{BNS}}(\{\mathbf{d}_i\}_{i=1}^{N_{\text{obs}}} | \mathbf{\Lambda}_{\text{BNS}})$ . The priors on the hyperparameters are the same as in Table I.

We find that the two posterior distributions are remarkably similar. This is a crucially different conclusion from the results shown in Ref. [S7] in the context of current GW detectors LIGO-Virgo-KAGRA (LVK). Putting together

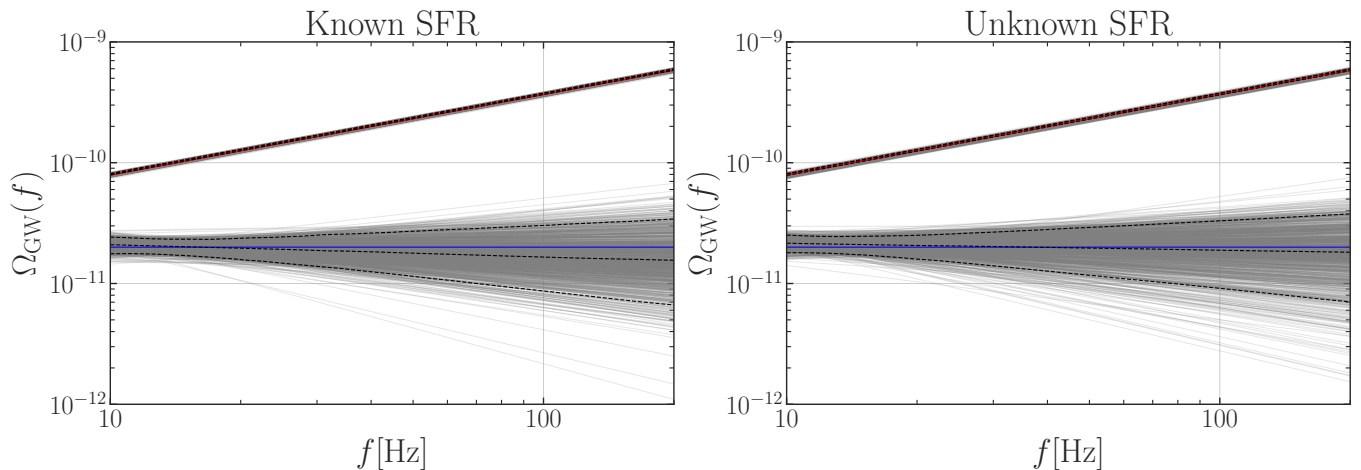


FIG. S5. Inferred energy density  $\Omega_{\text{GW}}$  of the BNS foreground and CGWB as a function of frequency in the two scenarios we consider. Each gray curve represents the resulting  $\Omega_{\text{GW}}(f)$  from a different posterior sample. The red straight line indicates the injected  $\Omega_{\text{GW}}(f)$  for the BNS foreground, while the blue line represents the injected  $\Omega_{\text{GW}}(f)$  for the CGWB. The dashed black curves depict the median and 90% quantiles.

data from the first two LVK observing campaigns (O1/O2), they found that constraints on the BBH merger rate significantly improve when including SGWB data in the population inference. In particular, constraints on the behavior of the merger rate at redshifts  $z \gtrsim 0.5$  were dominated by the stochastic search results. Their findings were primarily caused by the limited number of individual detections available ( $\sim 10$ ) and the fact that all of the detected events originate from BBHs in the local Universe. After increasing the number of individual BBH detections to 44 events by the first half of the third observing run (O3a), the LVK collaboration already found that constraints from direct detections begin to dominate over bounds from the stochastic foreground [S2]. In both of these cases, the information comes from the *non-detection* of the astrophysical SGWB. The expected *detection* of the SGWB from CBC with LVK at design sensitivity could once again provide improvements in the BBH merger rate constraints compared to individual detections [S2]. With XG detectors, however, our results suggest that the sheer number of detections, the higher detection fraction, and the larger redshift horizon imply that the constraints from individual detections completely dominate over the bounds from the SGWB, even for BNSs and with just 10 days of observation.

### C. Joint inference vs SGWB only

In Fig. S7 we compare posteriors on the BNS hyperparameters and CGWB parameters from the joint inference with posteriors resulting from an inference with SGWB data only. In other words, this time we compare inference results obtained from the full joint likelihood  $\mathcal{L}(\{\mathbf{d}_i\}_{i=1}^{N_{\text{obs}}}, \hat{C}^*(f) | \mathbf{\Lambda}_{\text{BNS}}, \mathbf{\Lambda}_{\text{CGWB}})$  of Eq. (S8) with results obtained just with the second term of the same equation,  $\mathcal{L}_{\text{SGWB}}(\hat{C}^*(f) | \mathbf{\Lambda}_{\text{BNS}}, \mathbf{\Lambda}_{\text{CGWB}})$ . For simplicity, we only show results for the more realistic case with unknown SFR. Once again, we adopt the same priors as in Table I.

We find that the constraints on all parameters are orders of magnitudes weaker when considering only SGWB data than with the joint inference. In particular, with a SGWB-only analysis, the marginalized 1D posterior on the CGWB amplitude  $\Omega_{\text{ref}}$  becomes fully consistent with  $\Omega_{\text{ref}} = 0$ , preventing us from claiming detection of the CGWB. This is caused by the fact that the BNS foreground completely dominates over the CGWB, as expected. The stringent constraints on the BNS merger rate from individual detections in the joint inference allow us to pin down the BNS foreground and to disentangle it from the CGWB, consistently with the discussion in the previous sections.

## IV. SANITY CHECK: ASSUMPTIONS ON THE JOINT LIKELIHOOD

Formally, the joint likelihood can be factorized in the form of Eq. (S8) if and only if the estimators of individual BNS signals and of the cross-correlation spectrum are independent random variables. Although these two analyses process raw data very differently, the cross correlation spectrum  $\hat{C}^*(f)$  also contains information from the individually

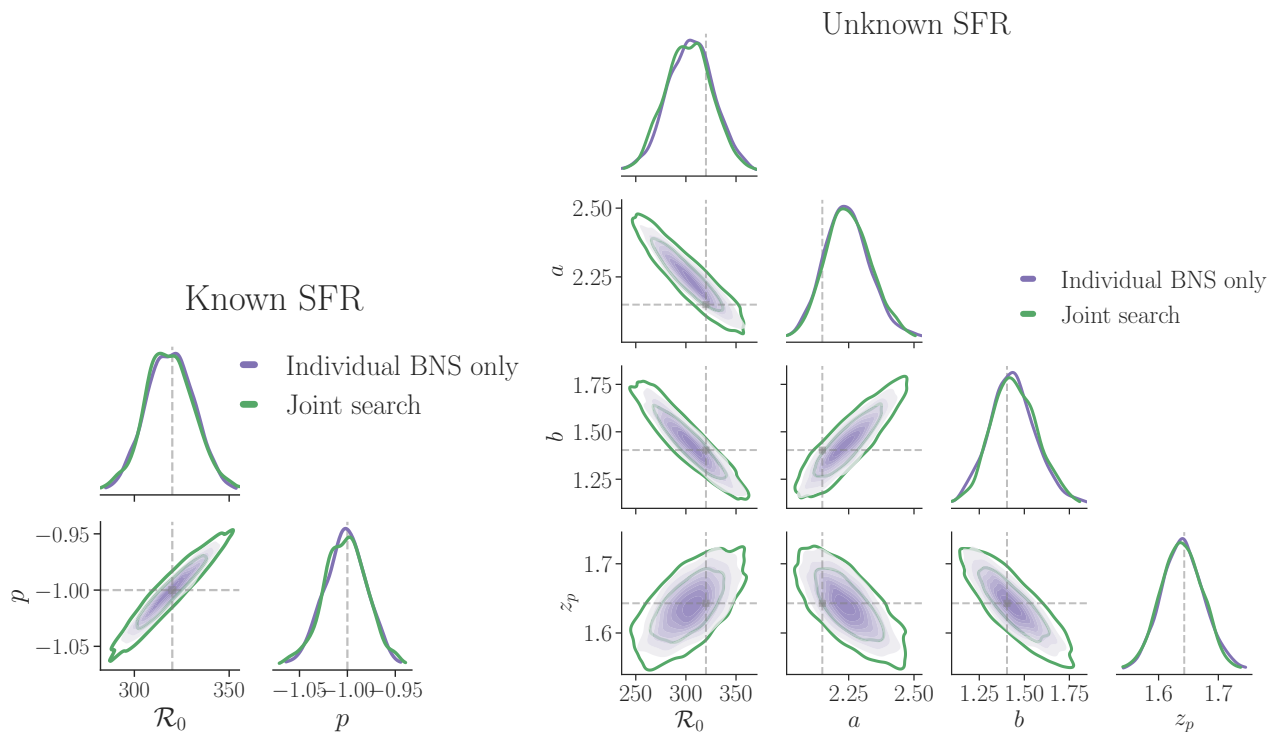


FIG. S6. Comparison between posteriors on the BNS hyperparameters resulting from the joint inference (green contours) and with individual BNS detection only (purple contours). The contours correspond to 68% and 95% of the probability, respectively. Results are shown for both the known (left corner plot) and unknown (right corner plot) SFR scenario.

resolved BNS signals, meaning that the two are not independent. Therefore, strictly speaking, Eq. (S8) can only be considered an approximation to the true joint likelihood for  $\{\mathbf{d}_i\}_{i=1}^{N_{\text{obs}}}$  and  $\hat{C}^*(f)$ .

To our knowledge, this issue has not been discussed in the literature before, neither in the paper that originally proposed this expression for the joint likelihood [S7], nor in subsequent applications by the LVK collaboration [S2]. With current GW detectors, the number of detected events  $\{\mathbf{d}_i\}_{i=1}^{N_{\text{obs}}}$  is so small compared to the total number of mergers that happen in the entire Universe (and thus enter  $\hat{C}^*(f)$ ), that the approximation is likely justified. As detectors keep improving and the fraction of individually resolved signals increases, it is unclear when Eq. (S8) will start to break down. In particular, with our population model and choice of XG detector network, we find that  $\sim 50\%$  of all the BNS signals are detected, meaning that the “double counting” of such signals in both  $\{\mathbf{d}_i\}_{i=1}^{N_{\text{obs}}}$  and  $\hat{C}^*(f)$  can potentially bias the inference.

To circumvent the issue and test the validity of the assumption in Eq. (S8), we propose a straightforward alternative approach that consists of partitioning the data into two independent sets. For example, if data from 20 days of observation are available, one can use data from the first 10 days exclusively for hierarchical inference on individual BNS detections  $\{\mathbf{d}_i\}_{i=1}^{N_{\text{obs}}}$ , and data from the remaining 10 days exclusively for the stochastic search to calculate  $\hat{C}^*(f)$ . This method is certainly suboptimal, as it does not make use of all the information in the data, but it ensures the joint likelihood can now safely be written in the form of Eq. (S8) without any approximation.

In Fig. S8 and Fig. S9, we compare results obtained by using the same dataset for both the hierarchical inference and stochastic search (i.e., the approach used in the rest of this study and in previous literature [S2, S7]) with results obtained with the novel approach just discussed, where the dataset is partitioned into two independent chunks. In practice, in the former case (labeled as *Single Analysis* in the figure) we simulate 10 days of data and use them both to calculate the cross-correlation spectrum  $\hat{C}^*(f)$  and to extract resolved BNS signals  $\{\mathbf{d}_i\}_{i=1}^{N_{\text{obs}}}$ . In the latter case (labeled *Half- $\mathcal{L}$ -Half*), we generate two independent realizations of 10 days of data and use one to compute  $\hat{C}^*(f)$ , and one to extract  $\{\mathbf{d}_i\}_{i=1}^{N_{\text{obs}}}$ . We then apply the same factorized joint likelihood of Eq. (S8) to both cases. Except small variations, the posterior distributions obtained via the two analyses are largely consistent with each other, both for the known and unknown SFR scenario. This suggests that using the same dataset for both terms in Eq. (S8) is a robust approximation for the purposes of our study, and any potential double counting does not significantly bias the inference.

We stress that this conclusion might change for different detector networks or population models, if the relative

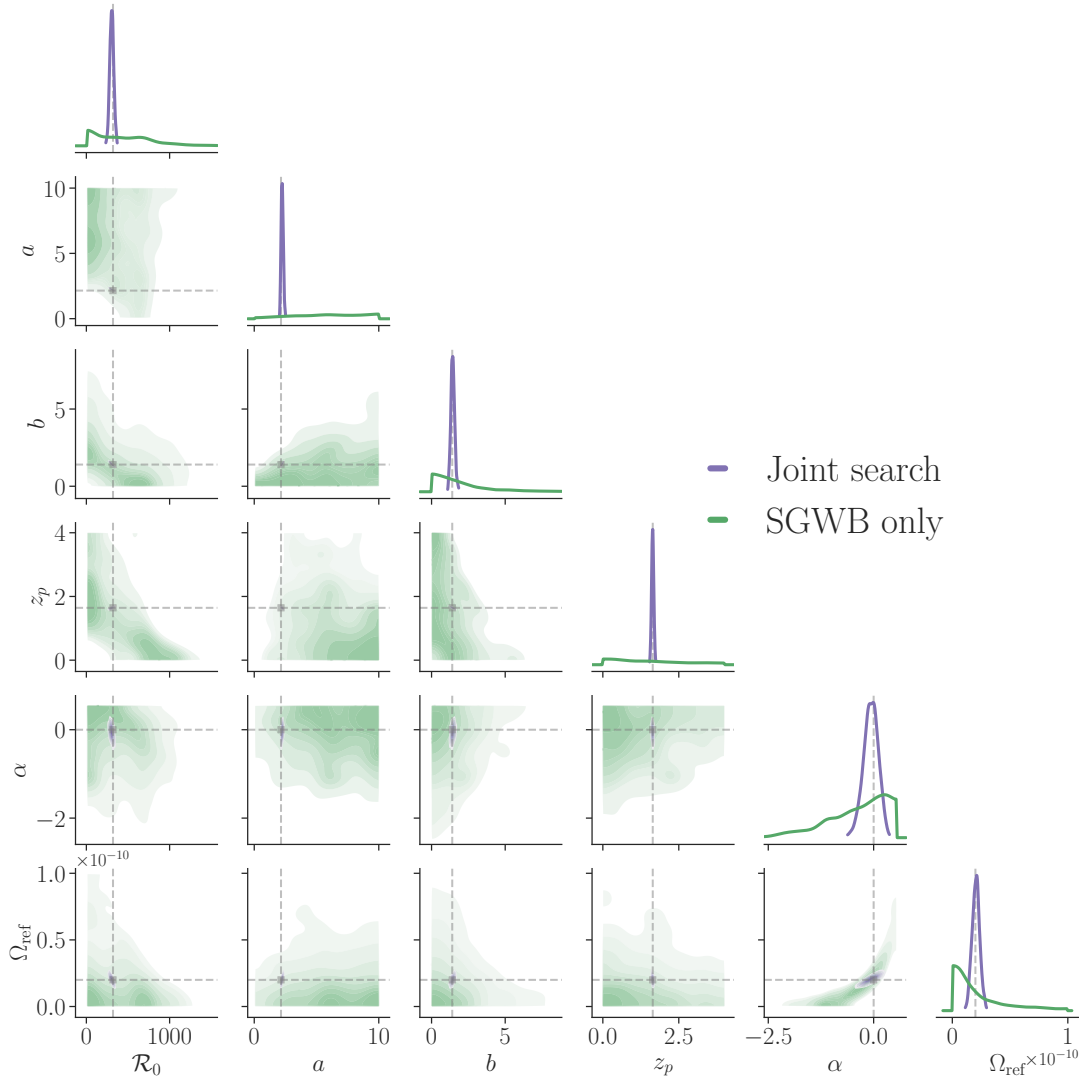


FIG. S7. Comparison between posteriors on the BNS hyperparameters and the CGWB parameters resulting from the joint inference (purple contours) and from SGWB data only (green contours). The contours correspond to 68%, and 95% of the probability mass, respectively. No prior knowledge of the SFR is assumed, other than its functional form.

constraining power of the two likelihood factors in Eq. (S8) differs significantly from our study. In such a case, the partitioning method proposed in this Section provides a viable and immediate solution. Different partition strategies can also be explored to identify the optimal split of the dataset, i.e., how much observation time to consider for the individual detections  $\{\mathbf{d}_i\}_{i=1}^{N_{\text{obs}}}$  versus the cross-correlation spectrum  $\hat{C}^*(f)$ . Finally, another way to ensure that the joint likelihood can be factorized into two independent contributions, as in Eq. (S8), is to further subtract the individually resolved BNS signals before computing  $\hat{C}^*(f)$ . If the subtraction residuals are negligible, this implies that only unresolved signals and the CGWB contribute to  $\hat{C}^*(f)$ , ensuring that it is independent from  $\{\mathbf{d}_i\}_{i=1}^{N_{\text{obs}}}$ . In this case, however, the expression for the SGWB likelihood of Eq. (S13) needs to be modified to account for selection effects, since the unresolved signals no longer represent a fair draw from the BNS population. We leave a more detailed exploration of these avenues to future work.

- 
- [S1] H. Zhong, B. Zhou, L. Reali, E. Berti, and V. Mandic, *Phys. Rev. D* **110**, 064047 (2024), arXiv:2406.10757 [gr-qc].  
[S2] R. Abbott *et al.* (KAGRA, Virgo, LIGO Scientific), *Phys. Rev. D* **104**, 022004 (2021), arXiv:2101.12130 [gr-qc].  
[S3] B. Allen and J. D. Romano, *Phys. Rev. D* **59**, 102001 (1999), arXiv:gr-qc/9710117.

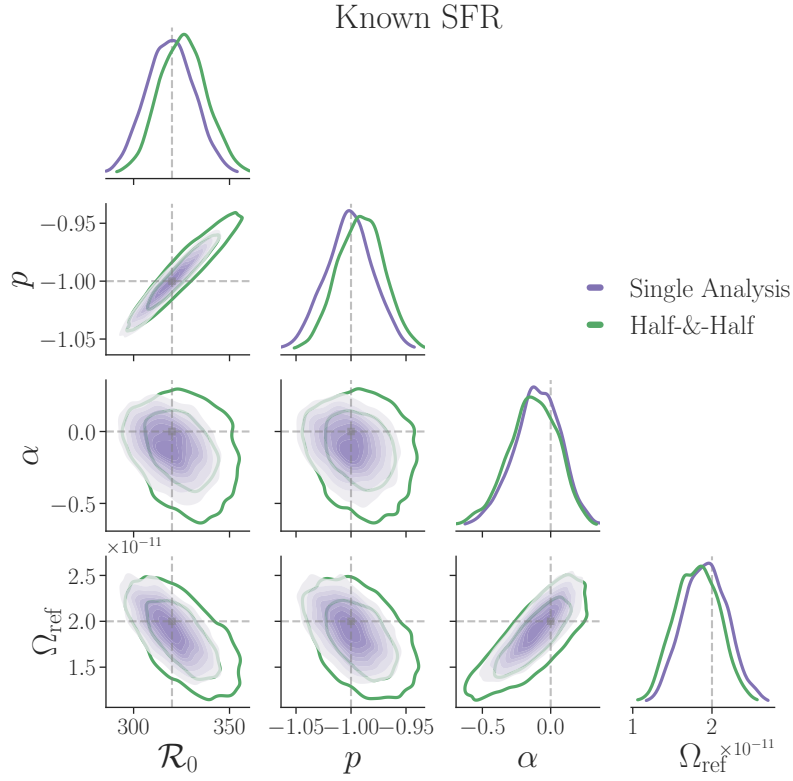


FIG. S8. Comparison of posterior distributions from *Single Analysis* (blue curves) and *Half-&-Half* (green curves) analyses for the known SFR scenario. The green contours correspond to 68%, and 95% of the probability mass, respectively.

- [S4] L. S. Finn, *Phys. Rev. D* **46**, 5236 (1992), arXiv:gr-qc/9209010.
- [S5] S. Borhanian, *Class. Quant. Grav.* **38**, 175014 (2021), arXiv:2010.15202 [gr-qc].
- [S6] H. Zhong, R. Ormiston, and V. Mandic, *Phys. Rev. D* **107**, 064048 (2023), [Erratum: Phys.Rev.D 108, 089902 (2023)], arXiv:2209.11877 [gr-qc].
- [S7] T. Callister, M. Fishbach, D. Holz, and W. Farr, *Astrophys. J. Lett.* **896**, L32 (2020), arXiv:2003.12152 [astro-ph.HE].
- [S8] I. Mandel, W. M. Farr, and J. R. Gair, *Mon. Not. Roy. Astron. Soc.* **486**, 1086 (2019), arXiv:1809.02063 [physics.data-an].
- [S9] S. R. Taylor and D. Gerosa, *Phys. Rev. D* **98**, 083017 (2018), arXiv:1806.08365 [astro-ph.HE].
- [S10] V. Mandic, E. Thrane, S. Giampanis, and T. Regimbau, *Phys. Rev. Lett.* **109**, 171102 (2012), arXiv:1209.3847 [astro-ph.CO].
- [S11] T. Callister, A. S. Biscoveanu, N. Christensen, M. Isi, A. Matas, O. Minazzoli, T. Regimbau, M. Sakellariadou, J. Tasson, and E. Thrane, *Phys. Rev. X* **7**, 041058 (2017), arXiv:1704.08373 [gr-qc].
- [S12] E. S. Phinney, (2001), arXiv:astro-ph/0108028.
- [S13] M. Fishbach, D. E. Holz, and W. M. Farr, *Astrophys. J. Lett.* **863**, L41 (2018), arXiv:1805.10270 [astro-ph.HE].
- [S14] M. Maggiore, *Gravitational Waves. Vol. 1: Theory and Experiments* (Oxford University Press, 2007).
- [S15] L. S. Finn and D. F. Chernoff, *Phys. Rev. D* **47**, 2198 (1993), arXiv:gr-qc/9301003.
- [S16] N. Aghanim *et al.* (Planck), *Astron. Astrophys.* **641**, A6 (2020), [Erratum: Astron.Astrophys. 652, C4 (2021)], arXiv:1807.06209 [astro-ph.CO].
- [S17] F. Iacovelli, M. Mancarella, S. Foffa, and M. Maggiore, *Astrophys. J.* **941**, 208 (2022), arXiv:2207.02771 [gr-qc].
- [S18] M. Vallisneri, *Phys. Rev. D* **77**, 042001 (2008), arXiv:gr-qc/0703086.
- [S19] M. Mancarella, F. Iacovelli, S. Foffa, N. Muttoni, and M. Maggiore, (2024), arXiv:2405.02286 [astro-ph.HE].
- [S20] U. Dupletsa, J. Harms, B. Banerjee, M. Branchesi, B. Goncharov, A. Maselli, A. C. S. Oliveira, S. Ronchini, and J. Tissino, *Astron. Comput.* **42**, 100671 (2023), arXiv:2205.02499 [gr-qc].
- [S21] S. R. Green and J. Gair, *Mach. Learn. Sci. Tech.* **2**, 03LT01 (2021), arXiv:2008.03312 [astro-ph.IM].
- [S22] M. Dax, S. R. Green, J. Gair, M. Pürerer, J. Wildberger, J. H. Macke, A. Buonanno, and B. Schölkopf, *Phys. Rev. Lett.* **130**, 171403 (2023), arXiv:2210.05686 [gr-qc].
- [S23] K. W. K. Wong, M. Isi, and T. D. P. Edwards, *Astrophys. J.* **958**, 129 (2023), arXiv:2302.05333 [astro-ph.IM].
- [S24] J. Alvey, U. Bhardwaj, S. Nissanke, and C. Weniger, (2023), arXiv:2308.06318 [gr-qc].
- [S25] K. Leyde, S. R. Green, A. Toubiana, and J. Gair, *Phys. Rev. D* **109**, 064056 (2024), arXiv:2311.12093 [gr-qc].



## Unknown SFR

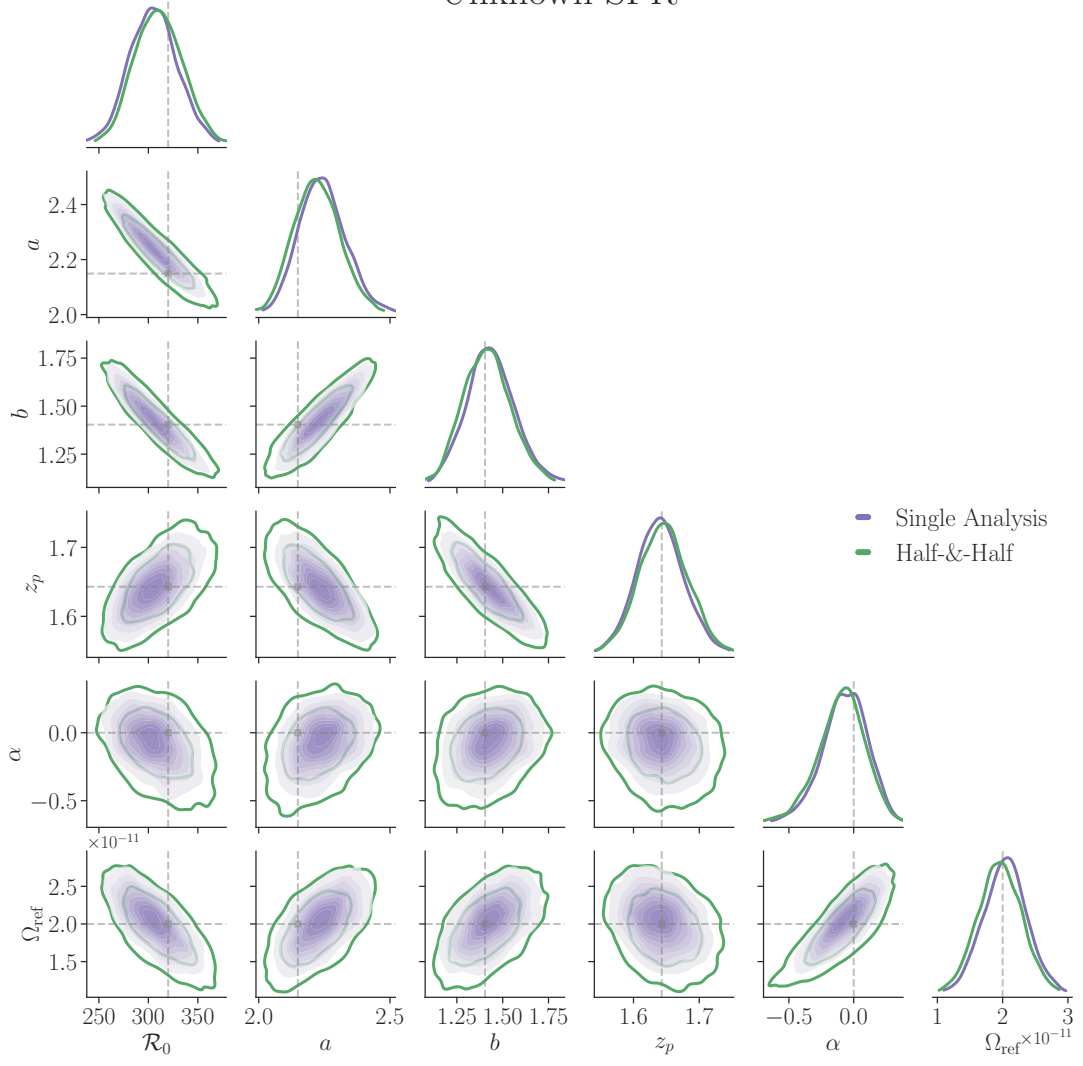


FIG. S9. Same as Fig. S8, but for the unknown SFR scenario.